On the use of dissolved oxygen isotopologues as biogeochemical tracers in the Pacific Ocean

Boda Li,[1] Huanting Hu,[1,2*] William M. Berelson,[3] Jess F. Adkins,[4] and Laurence Y. Yeung,[1,5*]

[1]Department of Earth, Environmental and Planetary Sciences, Rice University, Houston, TX 77005

[2]School of Oceanography, Shanghai Jiao Tong University, Shanghai 200240, China

[3]Department of Earth Science, University of Southern California, Los Angeles, CA 90089

[4]Division of Geological and Planetary Sciences, California Institute of Technology, Pasadena, CA 91125

[5]Department of Chemistry, Rice University, Houston, TX 77005

[*]Correspondence: haunting.hu@sjtu.edu.cn, lyeung@rice.edu

Abstract:

The isotopic composition of dissolved oxygen offers a family of potentially unique tracers of respiration and transport in the subsurface ocean. Uncertainties in transport parameters and isotopic fractionation factors, however, have limited the strength of the constraints offered by $^{18}O/^{16}O$ and $^{17}O/^{16}O$ ratios in dissolved oxygen. In particular, puzzlingly low $^{17}O/^{16}O$ ratios observed for some low-oxygen samples have been difficult to explain. To improve our understanding of oxygen cycling in the ocean's interior, we investigated the systematics of oxygen isotopologues in the subsurface Pacific using new data and a 2-D isotopologue-enabled isopycnal reaction-transport model. We measured $^{18}O/^{16}O$ and $^{17}O/^{16}O$ ratios, as well as the "clumped" $^{18}O^{18}O$ isotopologue in the northeast Pacific, and compared the results to previously published data. We find that transport and respiration rates constrained by O_2 concentrations in the oligotrophic Pacific yield good measurement-model agreement across all O_2 isotopologues only when using a recently reported set of respiratory isotopologue fractionation factors that differ from those most often used for oxygen cycling in the ocean. These fractionation factors imply that an elevated proportion of ^{17}O compared to ^{18}O in dissolved oxygen—i.e., its triple-oxygen isotope composition—does not uniquely reflect gross primary productivity and mixing. For all oxygen isotopologues, transport, respiration, and photosynthesis comprise important parts of their respective budgets. Mechanisms of oxygen removal in the subsurface ocean are discussed.

8450 words (main text)

561 words (figure captions)

9 Figures

2 Tables

Plain Language Summary

The marine biosphere produces and consumes oxygen, and in doing so, imparts fingerprints of photosynthesis and respiration (as well as other oxygen-consuming processes) on dissolved oxygen. These fingerprints are characterized by patterns in the abundances of istable isotopes ^{16}O, ^{17}O, and ^{18}O—versions of oxygen atoms that differ only in their atomic mass and do not decay over time. Dissolved oxygen contains two oxygen atoms, and thus has six different isotopic variants (e.g., $^{16}O^{16}O$, $^{16}O^{17}O$, and $^{16}O^{18}O$, among others). We report new measurements of five of these isotopic variants of molecular oxygen in the deep northeast Pacific Ocean and explain their patterns using a simplified model of oxygen transport and consumption. We find, contrary to prior reports, that all the isotopic fingerprints in the Pacific Ocean can be explained under a common framework without invoking unusual oxygen production, consumption, or transport mechanisms in the ocean. The results have implications for the use of oxygen isotopes as tracers of marine productivity, respiration, and transport, providing field evidence consistent with recent laboratory and theoretical studies of these isotopic fingerprints. Overall, the results suggest that revision of canonical isotopic fingerprints is warranted, affecting our understanding of biosphere productivity both in the present and past.

1. Introduction

1.1 Overview

Respiration and transport play fundamental roles in the chemical budgets of the subsurface ocean. Yet the myriad physical and biological processes comprising these budgets are challenging to resolve. Aerobic respiration remineralizes nutrients contained in organic matter, removes dissolved O_2 from seawater, and produces CO_2, while large-scale advection redistributes these constituents globally. Eddy diffusion operates in concert, decreasing concentration gradients on a smaller scale. Finally, ventilation at the surface drives the concentration of dissolved O_2 and CO_2 toward solubility equilibrium with the atmosphere. In principle, bioactive tracers like nutrients, dissolved inorganic carbon (DIC) and oxygen concentration can track features of these processes, but they cannot fully decouple respiration and transport in deep sea: distributions of nutrients and DIC vary stoichiometrically with oxygen concentration, and hence none of them provide independent constraints on respiration or transport (Takahashi et al., 1985).

Direct measurements of respiration rates in the deep sea are challenging because rates are slow and vary with location. Apparent oxygen utilization (AOU) can be combined with mean water mass ventilation ages to estimate oxygen utilization rates (OURs) (Feely et al., 2004). Mean water mass ages can be obtained through ocean circulation modeling (Riley, 1951; Craig, 1969; Haine & Hall, 2002), radiometric dating (e.g., ^{14}C of DIC) (Matsumoto, 2007; Koeve et al., 2015) or via the evolution of recently incorporated chemical constituents (e.g., chlorofluorocarbons) (Sonnerup, 2001). Implicit in the OUR method, however, are the assumptions that ventilation results in solubility equilibrium for O_2 and diffusive mixing influences AOU and age in the same way. The former is violated at high latitudes (Ito et al.,

2004), while the latter depends on the characteristic timescales of O_2 consumption and tracer decay. For example, a water mass at 50% O_2 saturation may have formed via closed-system respiration (i.e., OUR = AOU/age) or through mixing of many partially respirated water masses (i.e., OUR = $\Sigma f_i AOU_i/age_i$, where the AOU, age, and mixing fraction f of each constituent water mass i is not known) (Bender, 1990). Consequently, other tracers are needed to characterize the marine oxygen budget.

The distribution of O_2 isotopologues—the $\delta^{18}O$ value of O_2 in particular—has been used to disentangle respiration from transport, as closed-system respiration and mixing effects are distinguishable (Bender, 1990; Quay et al., 1993; Levine et al., 2009). Still, this single additional constraint has proven non-unique in part because reproducing $\delta^{18}O$-O_2 relationships requires independent knowledge of isotopic fractionation factors in the deep ocean. These fractionation factors may vary widely depending on environmental conditions such as diffusive limitation (Bender, 1990) or temperature (Stolper et al., 2018). Oxygen has three stable isotopes and O_2 has six stable isotopologues, however, so measurements of multiple O_2 isotopologues in the same sample of seawater may alleviate some of these uncertainties. Previous work on the triple-oxygen isotope composition of O_2 (i.e., $^{17}\Delta$ values, which are derived from $\delta^{18}O$ and $\delta^{17}O$ values; see Methods) has focused on estimating productivity in the surface ocean (Bender, 2000; Juranek & Quay, 2013; Luz & Barkan, 2000), although a few studies report data in the deep ocean.

Hendricks et al., (2005) reported the most extensive triple-oxygen dataset from the subsurface equatorial Pacific, which revealed some surprising and unexplained observations. First, non-monotonically varying $^{17}\Delta$ values in the aphotic zone were observed, peaking at moderate (50 - 80%) O_2 saturation, which were interpreted as a combination of photosynthesis in waters below the 1% light level and entrainment of productive waters. Second, some $^{17}\Delta$ values

97 at <50% O_2 saturation were unusually low and only explainable as two-component mixtures
98 between extreme endmembers (e.g., surface water and a ~5% O_2 saturation, highly respired
99 water mass). Moreover, recent experimental and theoretical evidence for variable isotopic
100 fractionation factors in the $^{17}\Delta$ system have offered alternate explanations for these data (Stolper
101 et al., 2018; Ash et al., 2020). The sensitivity of $^{17}\Delta$ values to photosynthesis, and uncertainty in
102 the relevant isotopic fractionation factors complicates their use as tracers of respiration and
103 mixing in the ocean.

104 The distributions of the remaining resolvable O_2 isotopologues in the ocean, $^{17}O^{18}O$ and
105 $^{18}O^{18}O$, have not yet been investigated. Yeung et al., (2015) and Ash et al., (2020) showed that
106 they are affected by photosynthesis and respiration, but in a manner different from either of the
107 singly-substituted isotopologues $^{16}O^{17}O$ and $^{16}O^{18}O$. In addition, physical fractionation
108 mechanisms such as diffusion lead to unique isotopologue patterns that can be distinguished
109 from those of photosynthesis and respiration (Li et al., 2019). This complementary sensitivity to
110 biogeochemical fractionation offered by these "clumped" isotopes, constrained by preliminary
111 isotopic fractionation factors, may facilitate a unified description of O_2 consumption and
112 transport in deep ocean.

113 Here we present new O_2 concentration and isotopologue data from northeast Pacific
114 ocean, from the surface into the aphotic zone. Bulk- (i.e., $\delta^{18}O$ and $^{17}\Delta$ values) and clumped-
115 isotope (i.e., Δ_{36} values reflecting $^{18}O^{18}O$) compositions were measured in the same dissolved O_2
116 samples for the first time to explore the potential utility of this suite of tracers to constrain
117 respiration and transport in the ocean. We further develop a 2-D isopycnal reaction-transport
118 model to examine the effects of respiration, photosynthesis, and transport on O_2 isotopologue
119 patterns in the Pacific. Finally, we revisit previous interpretations of deep-sea $\delta^{18}O$ and $^{17}\Delta$ data

and discuss the potential role of the recently proposed superoxide O_2 consumption pathway (Sutherland et al., 2020a) on the O_2 budget of the ocean.

2. Methods:

2.1 Isotope terminology and systematics

Dissolved O_2 isotopologue ratios are reported as $\delta^{18}O$, $^{17}\Delta$, and Δ_{36} values for $^{16}O^{17}O$, $^{16}O^{18}O$, and $^{18}O^{18}O$, respectively. The definitions of these terms are based on isotope/isotopologue ratios *R*. The denominator for *R* is the most abundant isotope or isotopologue (i.e., ^{16}O or $^{16}O^{16}O$), while the numerator is the rare isotope or isotopologue of interest. For example, the $^{18}O^{18}O$ isotopologue has a *R* value defined by

$$^{36}R = \frac{[^{18}O^{18}O]}{[^{16}O^{16}O]} \quad (1)$$

and is equal to the molar concentration of $^{18}O^{18}O$ divided by that of $^{16}O^{16}O$. Similar definitions are made for ^{18}R (i.e., $[^{18}O]/[^{16}O]$) and ^{17}R (i.e., $[^{17}O]/[^{16}O]$). The $\delta^{18}O$, $^{17}\Delta$, and Δ_{36} values are defined as

$$\delta^{18}O = \left(\frac{^{18}R_{sample}}{^{18}R_{air}} - 1\right) \quad (2)$$

$$^{17}\Delta = ln\frac{^{17}R_{sample}}{^{17}R_{air}} - 0.518 \times ln\frac{^{18}R_{sample}}{^{18}R_{air}} \quad (3)$$

$$\Delta_{36} = \left(\frac{^{36}R_{sample}}{^{36}R_{stochastic}} - 1\right) \quad (4)$$

with $\delta^{18}O$ and Δ_{36} values reported in per mil (‰) and $^{17}\Delta$ values reported in parts per million (ppm). The denominators relevant to $\delta^{18}O$ and $^{17}\Delta$ values are the *R* values for atmospheric O_2, which has been recently re-determined. Measurements at Rice University are consistent with the lab reporting Vienna Standard Mean Ocean Water-2 (VSMOW2) as $\delta^{18}O = -23.481‰$ and $^{17}\Delta = 204$ ppm relative to atmospheric O_2 (Wostbrock et al., 2020), which we will use subsequently in this manuscript. The denominator relevant to Δ_{36} values is defined by

$$^{36}R_{stochastic} = {}^{18}R^2 \quad (5)$$

and represents the $^{18}O^{18}O/^{16}O^{16}O$ ratio for a stochastic (random) distribution of isotopes within the sample being analyzed.

Biogeochemical cycling leads to a broad range of potential isotopic compositions in dissolved O_2. Isotopic fractionation due to respiration increases $\delta^{18}O$ and Δ_{36} values in the residual O_2 (Guy et al., 1993; Ash et al., 2020), but its effects on $^{17}\Delta$ values have recently been questioned: early work had initially suggested that $^{17}\Delta$ values do not change during respiration (Luz & Barkan, 2000; Angert et al., 2003; Helman et al., 2005; Luz & Barkan, 2005), but more recent work has argued that they may decrease (Stolper et al., 2018) or increase (Ash et al., 2020) in the residue fraction. The two-gyre model employed in this study uses the respiratory fractionation factors from Ash et al., (2020), as they were also measured in the Rice University laboratory and supported by first-principles calculations of enzymatic active-site analogues (see Table 1 and Section 2.3.2). Mixing relationships for $\delta^{18}O$ values are generally linear, but mixing relationships for $^{17}\Delta$ and Δ_{36} values are curved and may not be monotonic with mixing fraction (Miller, 2002; Eiler, 2007; Yeung et al., 2012). Nevertheless, the addition of photosynthetic O_2 into a dissolved pool of O_2 tends to decrease $\delta^{18}O$ and Δ_{36} values (Guy et al., 1993; Quay et al.,

1993; Yeung et al., 2015) and increase $^{17}\Delta$ values (Luz & Barkan, 2000, 2011). In principle, the combination of unique isotopic fractionation factors and mixing relationships for each isotopic system leads to a system of independent constraints on the history of a water parcel in the ocean, provided the fractionation factors for each biological process are known. In the deep ocean, the predominant mechanisms are respiration and mixing, although imprints of photosynthetic O_2 addition inherited from the surface ocean may also be present.

2.2 Water sampling and measurements of dissolved oxygen isotopologues

Ninety-four samples of dissolved O_2 for multi-isotopologue analysis were collected during a transect from Hawai'i to Alaska on R/V *Kilo Moana* during the Carbonate Dissolution In Situ Kinetics project in August 2017 (CDISK IV; see Fig. 1). Depth profiles were obtained at six sampling stations from the Hawai'i Ocean Time Series site (22.75˚N, 158˚W) up to the Gulf of Alaska (60˚N, 149.3˚W). Sampling methods followed those used previously for triple-oxygen isotope analysis of dissolved oxygen (Reuer et al., 2007). Briefly, Niskin bottles from a conductivity-temperature-depth rosette (CTD) were sampled into pre-evacuated ($<10^{-3}$ mbar), pre-poisoned glass bottles (1L, 2L, and 5L sizes depending on dissolved O_2 concentration with final $HgCl_2$ concentrations of >20 μg/mL seawater) that were each fitted with a Louwers-Hanique 9mm I.D. high-vacuum valve. During transport and storage before and after sampling, the side arm of the valve on each bottle was filled with water, with all visible bubbles removed, to minimize air contamination.

Gas extraction and analysis occurred at Rice University. Headspace gases were first collected onto silica gel fingers, with two U-shaped traps held at -196 °C upstream of the gel

finger to remove residual CO_2 and water vapor. The gases were then purified according to methods described previously, using an Agilent 7890B Gas Chromatograph (GC) held at −80 °C to separate O_2 from Ar, N_2, and other trace gases (Yeung et al., 2016). The O_2/Ar ratio was calculated using calibrated GC peak integration of O_2 and Ar, an approach that has a precision of ±4‰ (1σ) and shows good agreement with manometric checks performed in a calibrated volume (Ash et al., 2020). This ratio, relative to solubility equilibrium, was used to quantify dissolved O_2 saturation as reported herein; this biological supersaturation normalizes against physical disequilibria and is likely within several percent of the true dissolved O_2 saturation. It also allows one to focus on biological fractionation, reducing the scope of uncertainties relevant to measurement-model comparison. The purified O_2 was then analyzed for its isotopic composition on a high-resolution Nu Instruments *Perspective IS* isotope ratio mass spectrometer in dual-inlet mode. The pooled standard deviations for replicates within the CDISK IV dataset were ±0.20‰, ±5 ppm, and ±0.045‰ (1σ) for $\delta^{18}O$, $^{17}\Delta$, and Δ_{36} values, respectively.

2.3 Two-Gyre Model

Our 2-D advection diffusion reaction model is similar to the two-gyre models described in Levine et al., (2009) and Glover et al., (2011). We treat the Pacific ocean circulation as isopycnal in two dimensions because of the relatively strong mixing behavior within isopycnals and relatively weak diapycnal exchange (Bauer & Siedler, 1988; Glover et al., 2011). Ventilation occurs at high latitudes (~40°), where air-water equilibration resets dissolved gas concentrations and the isotopic signatures of dissolved O_2. There, we apply an equilibrium solubility and $^{18}O/^{16}O$ isotopic fractionation endmember corresponding to a sea surface temperature of 14˚C

(Benson & Krause, 1984; Li et al., 2019), which yields O_2 concentrations consistent with those observed in the ventilation region (see Table 1). The isotopic results are not sensitive to the particular choice of endmember, however, given the small overall isotopic fractionation at the air-sea interface.

2.3.1 Streamfunction

The 2-D isopycnal slab model contains two gyres: a cyclonic gyre to the south and an anticyclonic gyre to the north (Fig. 2 and S1). The model's advective geometry mimics the circulation observed in the North Pacific gyre between 0˚ and 40˚N that is composed of the Kuroshio Current, North Equatorial Current, North Pacific Current, and California Current, and the circulation observed in the South Pacific gyre between 0˚ and 40˚S that is composed of the Peru Current, South Equatorial Current and Antarctic Circumpolar Current. The streamfunction amplitude, *A*, which controls the absolute strength of advection in the isopycnal, was set to be consistent with the speed of the Kuroshio Extension and tuned using a cost function grid search (Section 2.3.3). The streamfunction asymmetry (i.e., driving stronger and narrower western boundary currents) was tuned to match the relative width of the Kuroshio current. Additional details, including the governing equations, can be found in Text S1.

2.3.2 Advection-Diffusion-Reaction Equations

Isopycnal advection, diffusion, and respiration can be generalized by eq. 6:

$$\frac{\partial C}{\partial t} = \nabla^2(KC) - \nabla \cdot (\boldsymbol{u}C) - J \quad (6)$$

where C is the concentration of the chemical species, K is the eddy diffusivity, and $\boldsymbol{u}$ is the advective velocity (i.e., a vector [u, v]), and J is the respiration rate. At each time step, eq. 6 was solved for a grid representing the subtropical gyres of the Pacific (e.g., 667 × 572 for σ_θ = 25.8 – 26.2) using inputs of A, K, and J and the second upwind differencing method (Glover et al., 2011).

In practice, the effects of transport and respiration are computed separately for each time step, with the respiration term computed after transport for each isotopologue. Respiration rates for the rare O_2 isotopologues are computed relative to that of $^{16}O^{16}O$ using their fractionation factors according to the equation below:

$$C_{res}^{t+1,rare} = C_{mix,no\ res}^{t+1,rare} - J * {}^{rare}\alpha * C_{mix,no\ res}^{t+1,rare} / C_{mix,no\ res}^{t+1,bulk} \quad (7)$$

Here, α is the isotopologue-specific respiration fractionation factor, i.e., the relative rate of consumption compared to that for $^{16}O^{16}O$ (Table 1). The α values for $^{16}O^{17}O/^{16}O^{16}O$ and $^{18}O^{18}O/^{16}O^{16}O$ fractionation are calculated from the mass-dependent exponents $\theta_{17/18,resp}$ and $\theta_{36/18,resp}$ of Ash et al., (2020) also shown in Table 1, using the equation:

$$ {}^{x}\alpha = \left({}^{18}\alpha\right)^{\theta} \quad (8)$$

where x = 17 or 36. The subscripts *no res* and *res* in eq. 7 denote the concentrations before and after the respiration step, respectively.

After updating the concentrations of the rare isotopologues, the model then updates the total O_2 concentration based on the total change in concentration of all isotopologues. If an O_2 isotopologue concentration is negative, it is set to zero, and if the $^{16}O^{16}O$ isotopologue

concentration is zero, all rare O_2 isotopologues are also set to zero. This approach avoids potential numerical instabilities associated with negative concentrations.

2.3.3 Model Parameter Initialization

The range of parameters considered for the isopycnal model are similar to those used for the south subtropical Atlantic (Levine et al., 2009). The σ_θ = 25.8 – 26.2 and 26.5 – 26.9 isopycnal layers were simulated because the former is near the median value for the measured samples, whereas the latter includes areas of lower O_2 saturation (i.e., 20 – 50%). Figure 3 shows the annual-mean depth and O_2 concentration for the σ_θ = 25.8 – 26.2 isopycnal derived from the World Ocean Atlas 2013 (WOA 2013; Locarnini et al., 2013, Zweng et al., 2013, Garcia et al., 2014). The ventilation region for the North Pacific subtropical gyre was set by approximating the areas of the isopycnal that lie within the mixed layer in the wintertime or 50m below; this seasonal variation is significant and has a strong influence on implied North Pacific respiration rates. The ventilation region in the South Pacific subtropical gyre was set by selecting the areas with depth <50m and >90% O_2 saturation in the annual mean because the seasonal variation has a negligible effect on the oxygen budget in the model North Pacific. These areas are shown as yellow rectangles in Fig. 2 for the σ_θ = 25.8 – 26.2 surface and Fig. S1 for the σ_θ = 26.5 – 26.9 surface.

Mass exchange between the northern and southern gyres is relatively small because the stream function is equal to zero at their boundary. Therefore, K at the boundary was set to be larger, particularly at the eastern and western edges of the tropical Pacific (see Tables 2 & 3). According to Cole et al., (2015), the horizontal eddy diffusivity is elevated near the equator, with the westernmost third having a horizontal eddy diffusivity of $10^{3.8}$ m^2/s at the surface. This eddy

diffusivity decreases with depth, and the data in Cole et al., (2015) imply a scaling factor of 0.8 for the σ_θ = 25.8 – 26.2 surface and 0.5 for the σ_θ = 26.5 – 26.9 surface, which yield K = 5040 m^2/s and 3150 m^2/s, respectively, for the westernmost region. The elevated equatorial eddy diffusivities for the central and easternmost third were calculated similarly and shown in Table 2. A grid search was employed to optimize the stream function amplitude A, the isotropic eddy diffusion coefficient K, and the respiration rate J (see Text S1).

Due of the unique biogeochemistry of the Pacific, with upwelling and high productivity near the equator and low productivity in the subtropical gyres, region-specific J values were utilized ($J_{equator}$ and J_{resp} for respiration within and outside the equatorial region, respectively). The equatorial upwelling region was delineated as the easternmost two-thirds of the area between -1000 km and 1000 km on the Y-axis of Fig. 5, which resembles the Pacific cold tongue. The oligotrophic regions comprised the rest of the model domain (±1000 km to ±4500 km on the Y-axis of Fig. 5). The stream function amplitude was varied within a range of flow velocities consistent with that observed for the Kuroshiro extension in the subsurface (Hall, 1989). The resulting optimized parameter set is shown in Table 2. The best-fit J_{resp} value for the σ_θ = 25.8 – 26.2 surface is 3.0 µmol/kg/yr, similar to the modeled value of 2.9 µmol/kg/yr for the σ_θ = 26.9 – 27.4 surface in the Atlantic reported in Levine et al., (2009) and the estimated value of 3 µmol/kg/yr reported in Feely et al., (2004) that was based on remineralization rates. The best-fit J_{resp} value for the σ_θ = 26.5 – 26.9 surface is 1.6 µmol/kg/yr, although there is significant uncertainty in this value because of both a strong dependence on size of the exposure area in the northwest Pacific and the larger depth range of the isopycnal (~800m). Nevertheless, the J_{resp} value is within the range prior estimates for these depths (Feely et al., 2004).

2.3.4 Model with photosynthesis

To simulate the effects of photosynthesis in the photic zone, we applied a photosynthetic flux signal to a 10 × 20 box region at the northwestern boundary of the model for the σ_θ = 25.8 – 26.2 surface. The flux is of pure O_2 with a composition of $\delta^{18}O$ = -20.172‰ and $\delta^{17}O$ = -10.275‰ relative to air, with Δ_{36} = -0.4‰, resulting in an admixture of photosynthetic and respired O_2 in the photic zone. We thus call this the "explicit addition" method. The photosynthetic endmember was calculated by first computing the $^{18}O/^{16}O$ and $^{17}O/^{16}O$ fractionation relative to VSMOW2 for "average phytoplankton" reported in (Luz & Barkan, 2011)—i.e., $^{18}\alpha$ = 1.003389 and $^{17}\alpha$ = 1.001778. These fractionation factors were then applied to VSMOW2 as the source water [$\delta^{18}O$ = -23.481‰ and $\delta^{17}O$ = -12.031‰ relative to air (Wostbrock et al., 2020)]. The goal of this scheme is to use the photosynthetic isotope fractionation from (Luz & Barkan, 2011), but to scale the isotopic composition of O_2 to be consistent with $^{17}\Delta$ measurements made in our lab (Yeung et al., 2018; Pack et al., 2016; Wostbrock et al., 2020). The Δ_{36} value of photosynthetic O_2 was estimated from preliminary measurements (Yeung et al., 2015), but the results are not sensitive to its precise value near Δ_{36} = 0. The maximum amount of photosynthetic O_2 added into the system was equivalent to +60% saturation, which, while not typically present in the ocean, were used to evaluate the range of the possible admixtures of photosynthetic and respired O_2. We note that this implementation does not include explicit biogeochemical cycling of photosynthetic O_2 within the photic zone, which results in an accumulated triple-oxygen isotope signature from photosynthetic O_2 addition and partial respiration of the admixture. Instead, those effects are represented schematically alongside the model results.

Using the same approach for the smaller ventilation region of the σ_θ = 26.5 – 26.9 surface yielded negligible changes to the isotopologue patterns, so an second approach was also used to simulate the effects of photosynthesis, following that used in an earlier 3D model simulation (Nicholson et al., 2014). Rather than adding in photosynthetic O_2 explicitly, photosynthetic O_2 was added implicitly by changing the ventilation boundary condition to be representative of the mixed-layer isotopologue compositions measured during CDISK4, namely, $\delta^{18}O$ = 0.36‰, $^{17}\Delta$ = 30 ppm, and Δ_{36} = 1.90‰. The largest effect of this "implicit addition" method is to elevate $^{17}\Delta$ values from equilibrium (i.e., above 8 ppm), although overall the effects remain subtle and sufficient for illustrative purposes.

3. Results:

3.1 Isotopic measurements

The CDISK4 data span the oligotrophic and subarctic Northeast Pacific (Fig. 1) at depths ranging from the surface to 3000 m (σ_θ = 20.7 – 27.8), and show consistent patterns associated with biogeochemical processing. At the Hawaii Ocean Time Series site (CDISK4-S1), for example, dissolved O_2 saturation generally decreases, while $\delta^{18}O$ and Δ_{36} values generally increase with increasing depth except towards the base of the oxygen minimum zone (1486m sample; Fig. 4). These trends are associated with respiratory isotopic fractionation, which increases $\delta^{18}O$ and Δ_{36} values in the residual O_2 (Guy et al., 1993; Ash et al., 2020). The $^{17}\Delta$ and Δ_{36} values also show prominent photosynthetic signals: $^{17}\Delta$ values are elevated at the top of the thermocline, while Δ_{36} values are lowered, owing to the accumulation of photosynthetic O_2 that has been partially respired (Luz & Barkan, 2000, 2009; Yeung et al., 2015). In the mixed layer,

331 the $^{17}\Delta$ and Δ_{36} values of O_2 approach atmospheric values, consistent with gas exchange driving
332 the isotopic composition of O_2 toward solubility equilibrium with the atmosphere (Knox et al.,
333 1992; Li et al., 2019).

334 The $\delta^{18}O$ and Δ_{36} data increase as dissolved O_2 concentrations decrease, from values
335 below solubility equilibrium (-0.6‰ and 1.5‰ with some variability, respectively) to values
336 much higher than those in air (18‰ and 3.1‰, respectively), with little variance about their
337 curvilinear trends. The $^{17}\Delta$ data, however, show more variable behavior: near the surface, $^{17}\Delta$
338 values range from 21 – 118 ppm, whereas at low O_2 concentrations (< 40% saturation) they
339 range from 50 – 100 ppm. In effect, the $^{17}\Delta$ data envelope appears to narrow with decreasing O_2
340 concentrations, with a pronounced increase in minimum values, although the narrowing may
341 simply reflect the locations sampled. The Δ_{36} data show no discernable trend toward local
342 isotopic equilibrium, which would range from 1.77‰ (2°C) to 1.49‰ (27°C) in these waters.
343 These data are plotted and compared with the two-gyre model results in Section 4.1.

344

345 **3.2 Two-Gyre Model**

346 The model domain is generally ventilated near the Northwest corner and along the entire
347 Southern edge, with some interhemispheric mixing, leading to different systematics in the
348 Northern and Southern gyres. We illustrate the general features of these advection-diffusion-
349 respiration trajectories on the σ_θ = 25.8 – 26.2 surface below. Three specific regions are
350 highlighted in Fig. 5; their advection-diffusion-respiration arrays are shown in Fig. 6.

351 In the northwest corner, the advective direction is clockwise, whereas the direction of
352 eddy-diffusive transport of O_2 is primarily counter-clockwise. Oxygen concentrations decrease

from the northeast to the southwest, driving net diffusive transport along this gradient. Advection and diffusion thus drive O_2 transport in opposing directions. At steady state, the O_2 fluxes F in this region satisfy the following relationship:

$$|F_K| = |F_A| + |F_R| \quad (9)$$

Here, the subscripts refer to the contributions from eddy diffusion (K), advection (A), and respiration (R). Because F_R is small (3.0 μmol O_2/kg seawater/yr) and the O_2 gradient is relatively large, the O_2 budget has a large contribution from diffusive-advective mixing between high- and low-O_2 waters. The effects on the isotopic composition of O_2 therefore trend toward that of two-endmember mixing between high- and low-saturation waters; in Fig. 6, the isotopic trends in the northwest region resemble those predicted for mixing between surface waters and Rayleigh-fractionated waters at ~30% O_2 saturation, as implied by Fig. 5.

In the northeast, the O_2 flow pattern changes: advection and eddy diffusion drive O_2 transport in a similar direction (counterclockwise). At steady state, the O_2 fluxes therefore satisfy the relationship:

$$|F_R| = |F_A| + |F_K| \quad (10)$$

Both the advective and eddy-diffusive fluxes (cf. Fig. 2 and the concentration gradient in Fig. 5) are smaller in this region, balancing the small respiration flux. Changes in O_2 saturation in this region are therefore more strongly affected by respiratory consumption, resulting in an isotopic pattern that trends closer to Rayleigh fractionation, at least compared to the Northwest Pacific: the relatively weak advection and diffusion makes this region show more closed-system behavior.

In the southern gyre, advection is counterclockwise, and the concentration gradients are weaker owing to a larger exposure surface for the isopycnal. The mixing pattern in the southeast

is similar to that of the northeast, with advection and diffusion in the same direction, resulting in a Rayleigh-like isotopic fractionation pattern; however, the O_2 saturation range is smaller than in the northeast, so that portion of the array does not appear prominently in Fig. 6. In the southwest, the mixing patten is similar to the northwest, where the large O_2 concentration gradient leads to isotopic trends closer to those for two-endmember mixing.

These basic systematics suggest that the model results can be understood as a continuum of water parcels lying somewhere between the trends expected from closed-system Rayleigh fractionation and two-endmember mixing between low- and a high-O_2 endmembers, with region-specific patterns reflecting the local budget. For example, the σ_θ = 26.5 – 26.9 surface reflects a more complex mixture likely involving more than two mixing endmembers (cf. Fig. S3). The range in the observational data should nevertheless constrain the range of low-O_2 endmembers that contribute to the subsurface Pacific O_2 budget.

Ultimately, the simulated $\delta^{18}O$, $^{17}\Delta$, and Δ_{36} values are all anticorrelated with O_2 saturation because of the tendency for respiration to consume light oxygen isotopologues. For $^{17}\Delta$ values, the trend with O_2 saturation is controlled by the particular mass-dependent fractionation slope for respiration used (see Table 1): the $\theta_{17/18,resp}$ value of 0.520 used in these simulations is larger than the reference slope of λ = 0.518 used to define $^{17}\Delta$, resulting in an increase in $^{17}\Delta$ values as O_2 saturation decreases. Similarly, the mass-dependent fractionation slope for $^{18}O^{18}O$ relative to $^{16}O^{18}O$, $\theta_{36/18,resp}$ = 2.048, is larger than the slope that would preserve Δ_{36} values upon Rayleigh fractionation (i.e., $\theta_{36/18}$ = 2.000), resulting in an increase in Δ_{36} values as O_2 saturation decreases.

Modeled $^{17}\Delta$-$\delta^{18}O$ and Δ_{36}-$\delta^{18}O$ correlations are generally positive with modest variability about overall curvilinear trends (Fig. 6 D-F). Compared to isotopologue-O_2 saturation plots (Fig. 6 A-C), the model results for the northwest region in these isotopologue cross-plots adhere closer to the expected trajectories for two-endmember mixing. This observation indicates that the departures from the mixing trajectories in Fig. 6 A-C are mainly due to minor contributions from lower-O_2 waters.

The apparent mass dependence resulting from isopycnal transport, mixing, and respiration resembles Rayleigh fractionation with $\theta_{17/18,resp} < 0.520$ and $\theta_{36/18,resp} > 2.048$—i.e., different from the process-level values—mainly because curvilinear mixing trajectories for $^{17}\Delta$ and Δ_{36} values (Miller, 2002; Eiler, 2007; Yeung et al., 2012) draw the model array away from pure Rayleigh-like trends. These deviations from the process-level mass-dependent fractionation slopes for respiration resemble the deviations observed in $\delta^{18}O$ data reported here and in previous work (Bender, 1990; Levine et al., 2009). For example, a respiratory fractionation factor of $^{18}\alpha = 0.982$ yielded model results having an apparent Rayleigh fractionation factor of $^{18}\alpha = 0.990$ in the subtropical Atlantic (Levine et al., 2009). Notably, however, Rayleigh fractionation and two-endmember mixing yield nearly coincident trajectories for Δ_{36} values when plotted against O_2 saturation (Fig. 6C), leading to minimal spread in the model results compared to the other isotopologue tracers.

The addition of photosynthetic O_2 to a small surface-outcropping region in the northwest corner of the $\sigma_\theta = 25.8 – 26.2$ surface results in higher O_2 concentrations throughout the isopycnal and a larger range of predicted isotopic compositions compared to the respiration-only scheme. The largest spread in isotopic composition occurs at high O_2 saturation; however, these compositions converge toward the respiration-only results as O_2 saturation decreases because of

signal dilution and respiration within the aphotic zone. These general observations will be discussed further in the measurement-model comparison below.

4. Discussion:

4.1 Comparison of measurements and the model

4.1.1 CDISK4 data

The CDISK4 data are compared with the simulated isotopologue compositions in the Northeast region of the isopycnal model in Figs. 7 (respiration only) and 8 (with photosynthetic O_2). The model predicts the general increase in $\delta^{18}O$, $^{17}\Delta$, and Δ_{36} values as O_2 saturation decreases, as well as much of the isotopic covariation observed in the CDISK4 data. Importantly, the narrowing range of $^{17}\Delta$ values observed at mid-saturation in the CDISK4 data (i.e., ~60%) is reproduced in both the respiration-only isopycnal model and the model that includes photosynthetic O_2. We note that multiple photosynthesis-respiration cycles taking place in the photic zone (as opposed to the single-step addition of photosynthetic O_2 modeled above) would yield a "zig-zag" pattern that increases $^{17}\Delta$ values and decreases Δ_{36} values with little change in O_2 saturation (schematically shown in Fig. 8). The magnitudes of these displacements depend on the relative rates and extents of photosynthesis-respiration cycling and mixed-layer ventilation, as well as the precise values of the mass-dependent exponents for respiration used. While $\delta^{18}O$ values are also affected by these cycles, the effects are smaller and nearly collinear, resulting in limited scatter in the data (Fig. 8A).

Broadly, these results suggest that the mean respiratory fractionation factors in the deep Pacific, and in particular, the mass-dependent exponents, are consistent with those obtained from

441 freshwater incubation experiments in our laboratory, i.e., $\theta_{17/18,resp} > 0.518$ and $\theta_{36/18,resp} > 2$ (Ash
442 et al., 2020). By contrast, the CDISK4 data cannot be explained satisfactorily by the other triple-
443 oxygen exponents previously reported (e.g., $\theta_{17/18,resp} = 0.516$ shown in Fig. S4), which have
444 assumed $\theta_{17/18,resp} \leq 0.518$ (Luz & Barkan, 2000; Angert et al., 2003; Helman et al., 2005; Luz &
445 Barkan, 2005; Stolper et al., 2018).

446 The measurement-model disparities in $^{17}\Delta$ and Δ_{36} values at high O_2 saturation are worth
447 discussing. The data show a large range in $^{17}\Delta$ and Δ_{36} values at shallow depths (i.e., low
448 potential density σ_θ and near O_2 solubility equilibrium) that are clearly associated with
449 photosynthesis, but which are not necessarily reproduced by the model containing a simple
450 photosynthetic O_2 source. Multiple photosynthesis-respiration cycles are required to explain the
451 range of $^{17}\Delta$ values observed at shallow depths. This cycling has a pronounced impact on
452 $^{17}\Delta$ values because both respiration ($\theta_{17/18,resp} > 0.518$) and photosynthesis increase the $^{17}\Delta$ value
453 of dissolved O_2. For Δ_{36} values, however, photosynthesis and respiration have opposing effects,
454 leading to a different cumulative effect on Δ_{36} values. Respiration increases Δ_{36} values, while the
455 addition of photosynthetic O_2 draws down the Δ_{36} value of the dissolved O_2 pool. The presence
456 of photosynthetic O_2 may still be detectable in the data because the Rayleigh fractionation and
457 photosynthetic O_2 mixing vectors are not collinear.

458 The lowest measured Δ_{36} values can be explained by the particular mixed-layer O_2
459 cycling scenario presented in Fig. 8. However, the maximum observed $^{17}\Delta$ values are as much as
460 50 ppm higher than the mixed-layer O_2 cycling scenario predicts. Increasing productivity alone
461 would yield better agreement for $^{17}\Delta$ values, but cause disagreements in Δ_{36} values. Therefore,
462 this disparity may arise from uncertainties in the mass-dependent slopes for respiration and/or an

463 incomplete accounting of oxygen consumption in the mixed layer. A higher $\theta_{17/18,resp}$ value in the
464 mixed layer (i.e., greater than 0.520), for example, could help resolve the $^{17}\Delta$-Δ_{36} disparity, as it
465 would lead to larger increases in $^{17}\Delta$ values when oxygen is consumed. A larger $\theta_{36/34,\,resp}$ value
466 (i.e., greater than 2.048) could also help resolve this disparity. Using a higher $\theta_{36/18,\,resp}$ value, the
467 trajectories of Rayleigh fractionation and photosynthetic O_2 addition are closer to collinear,
468 resulting in a smaller net decrease in Δ_{36} values per cycle in the photic zone. We note that the
469 isopycnal model was implemented to reproduce large-scale O_2 isotopologue trends in the open
470 ocean rather than specific features of the surface isotopologue budget. Phenomena such as the
471 seasonal accumulation of photosynthetic signals below the mixed layer (Luz & Barkan, 2009)
472 are more sensitive to subtle differences in respiratory fractionation factors. Consequently, we
473 consider the small $^{17}\Delta$ excesses (e.g., 10 – 20 ppm) or Δ_{36} deficits (e.g., 0.1 – 0.2‰) to be
474 consistent with the model, as they likely reflect preservation of these near-surface signals.

475 At low O_2 saturation (i.e., < 50%), we find mostly good agreement, with measurement-
476 model disparities primarily in $\delta^{18}O$ values. These data are more sensitive to and potentially more
477 influenced by diapycnal mixing, which would draw the isotopic data along endmember mixing
478 trajectories with neighboring isopycnal surfaces (akin to the systematics of the northwest Pacific
479 described in Section 3.2.1). Diapycnal O_2 concentration gradients across isopycnal surfaces can
480 be strong, especially in the northeast Pacific (e.g., ~50% between the σ_θ = 25.8 – 26.2 and σ_θ =
481 26.5 – 26.9 surfaces), so the O_2 budget on the isopycnal may be incomplete at lower O_2
482 saturation. Previous studies also suggest that the effective isotopic discrimination may be weaker
483 at depth, perhaps related to diffusion limitation in particles or in sediments (Bender, 1990;
484 Levine et al., 2009). Our results do not rule out this possibility: changing the $^{18}\alpha_{resp}$ to 0.986
485 (from 0.982) improves agreement between the model and measurements in the lower range of O_2

saturation for the σ_θ = 26.5 – 26.9 surface, although the model results near 50% show poorer agreement. Agreement for the other isotopologues is comparable in both cases.

4.1.2 Previously published northeastern Pacific and equatorial Pacific data

We now compare our results with those of earlier studies on $\delta^{18}O$ and/or $^{17}\Delta$ of O_2 in the deep Pacific. Three previous studies are relevant. The first is Quay et al., (1993), which reports data from Stations Papa (50˚N 145˚W) and R (53˚N 145˚W). These two stations are subarctic and not in the model domain (40˚N to 40˚S), but they are close to the CDISK4-S5 and CDISK-S7 sites. The second study is Hendricks et al., (2005), which reports data from the equatorial Pacific, a productive environment influenced by upwelling. The third study is Quay et al., (2010), which includes data from the aphotic zone of the Hawaii Ocean Time Series site. Other studies from the Pacific [e.g., (Juranek & Quay, 2010; Juranek et al., 2012; Haskell et al., 2017)] were omitted for clarity because they were either coastal or did not report O_2 isotopologue measurements from below the mixed layer. While seasonal biases between studies may be important, aphotic-zone trends are less likely to be sensitive to sampling season: the convergence of isotopic data at low O_2 saturations suggests that lower-oxygen regions have a muted sensitivity to short-term surface variability in part due to dilution. The $^{17}\Delta$ values were recalculated according to eq. 3 and the results are shown alongside the CDISK results in Figs. 7, 8 and 9.

The Quay et al. (1993) North Pacific $\delta^{18}O$ data are comparable to the CDISK4 data; both are well explained by the isopycnal model. Some outliers in the data are apparent, but may reflect localized conditions and/or subtle sample contamination. The equatorial Pacific data from

Hendricks et al., (2005), however, show a much larger spread in $\delta^{18}O$ and $^{17}\Delta$ values than the CDISK4 data. At high O_2 saturation, the Hendricks et al. (2005) data largely resemble the CDISK4 data, with higher $^{17}\Delta$ values reflecting higher productivity in the equatorial upwelling region. The lower ranges of the Hendricks et al. (2005) $\delta^{18}O$ and $^{17}\Delta$ data, however, lie below the two-endmember mixing line (1%-100% saturation), with some water samples showing $^{17}\Delta$ values lower than even that for solubility equilibrium. Moreover, the $^{17}\Delta$ signals peak near moderate O_2 saturations rather than at high O_2 saturations in the equatorial Pacific. This high-$^{17}\Delta$ pattern, accompanied by low $\delta^{18}O$ values, is still apparent when O_2 saturation is low (~20%). The isotopic differences between the equatorial and northeast Pacific at low O_2 saturation are too large to be explained by differences in model parameters (Figs. 8D & 9D).

These observations suggest that the high productivity and respiration rates in the equatorial Pacific yield fundamentally different O_2 isotopologue systematics than in the northeast Pacific, even in the subsurface. To explain these systematics, we will first summarize the original explanation of the data put forth by Hendricks et al., (2005). The data were separated into three bins: (*i*) the mixed layer, (*ii*) the thermocline in the euphotic zone, and (*iii*) the aphotic zone. The mixed-layer data were explained by a conventional flux balance of photosynthesis, respiration, and air-sea gas exchange, whereas the other two bins required inputs of photosynthetic O_2 where light levels have traditionally been considered too low to support significant primary productivity. In particular, the high-$^{17}\Delta$/low-$\delta^{18}O$ pattern at moderate O_2 saturation in the thermocline, as well as the non-monotonic trends in $^{17}\Delta$ below the mixed layer (Fig. 9), were attributed to a combination of diapycnal mixing and local photosynthesis near or even below the 1% light level.

However, at the time, increases in $^{17}\Delta$ values were thought only to arise from the addition of photosynthetic O_2. The CDISK4 data and modeling results, as well as a recent study, suggest

that $^{17}\Delta$ values can also increase as O_2 is consumed by respiration (Ash et al., 2020). Respiration-driven $^{17}\Delta$ increases at the surface and in the ocean's interior offer an alternate explanation for the isotopic trends seen in the equatorial Pacific.

For example, the high-$^{17}\Delta$/low-$\delta^{18}O$ pattern near 50% O_2 saturation in the euphotic thermocline does not require an unusual amount of sub-mixed layer photosynthesis, at least relative to what has been observed elsewhere (Luz & Barkan, 2009); respiration and diapycnal inputs of mixed-layer O_2 can explain the trend. The productive cold tongue sits above a shallow oxygen minimum in the equatorial Pacific, facilitating diapycnal mixing between productive and respired waters (i.e., between high- and low-O_2 endmembers that both have high $^{17}\Delta$ values) (Hendricks et al., 2005). The equatorial Pacific $\delta^{18}O$ data generally fall closer to a 1% – 100% two-endmember mixing curve compared to the northeast Pacific data (Fig. 7A), supporting a greater role for mixing across a large O_2 gradient. Therefore, two-endmember mixing between waters at the subsurface $^{17}\Delta$ maximum and waters with low O_2, combined with respiration, can explain this high-$^{17}\Delta$/low-$\delta^{18}O$ pattern at moderate O_2 saturation in the equatorial Pacific. Photosynthesis at depths below the 1% light level is not required to explain these data.

At lower O_2 saturation (<50%), many $^{17}\Delta$ values from the equatorial Pacific are unexpectedly low, with several even being negative, although negative $^{17}\Delta$ values were also found in the photic zone. Similarly low $^{17}\Delta$ values at low O_2 saturation were reported by Haskell et al., (2017) at the coastal San Pedro Ocean Time Series site (33˚33'N, 118˚24'W). These low $^{17}\Delta$ values do not appear in the CDISK4 data, nor do they appear in any of the model scenarios.

Observations of low $^{17}\Delta$ values in the ocean are usually explained by mixing between near-surface waters and an extremely low-O_2, pure-Rayleigh respiration endmember [e.g., ~5%

553 O_2 saturation using $\theta_{17/18,resp}$ = 0.518 (Nicholson et al., 2014)]. Less extreme endmembers cannot
554 reproduce those data because the nonlinearity in mixing for $^{17}\Delta$ values is insufficient. We note
555 that no datasets in the Pacific thus far have shown low-O_2 samples near the Rayleigh
556 fractionation curve for surface waters: for example, the lowest O_2 saturation observed in the
557 CDISK4 dataset is 6% (CDISK4-S2, 849m depth), and duplicate isotopic measurements showed
558 $\delta^{18}O$ values of 18.27‰ and 18.32‰ and Δ_{36} values of 3.14‰ and 3.13‰, which are lower than
559 the values predicted for Rayleigh fractionation ($\delta^{18}O$ = 52.74‰ and Δ_{36} = 3.40‰ using $^{18}\alpha_{resp}$ =
560 0.982 and $\theta_{36/18,\,resp}$ = 2.048). The measured $^{17}\Delta$ values (82 ppm and 87 ppm) are also higher than
561 the presumed low-O_2 endmember $^{17}\Delta$ value used by Nicholson et al., (2014) of 40 ppm. The
562 elevated $^{17}\Delta$ value characteristic of the highly respired endmember renders a negative $^{17}\Delta$ value
563 more difficult to obtain. Using $\theta_{17/18,\,resp}$ = 0.520 (Ash et al., 2020), a Rayleigh-like mixing
564 endmember of <5% O_2 saturation would be required to explain negative $^{17}\Delta$ values (Fig. 9).

565 Recent studies suggest that temperature-dependent isotopic fractionation factors (Stolper
566 et al., 2018) and analytical artifacts (Yeung et al., 2018) may contribute to these signals.
567 However, the waters sampled during CDISK4 range from 2°C to 27°C, yet show minimal
568 change in isotopic systematics with temperature; temperature-dependent isotopic fractionation
569 factors need not be invoked to explain the multi-isotopologue trends. Finally, we note that
570 contamination by atmospheric O_2 cannot explain the observed deviation from the Rayleigh
571 fractionation curve because the disparities in $\delta^{18}O$, $^{17}\Delta$, and Δ_{36} values are not consistent (e.g.,
572 the $\delta^{18}O$ deviation would indicate that the sample is 65% air and the Δ_{36} deviation would indicate
573 the sample is 19% air). While we cannot strictly rule out contamination of the CDISK4 data, the
574 repeatability and consistency in isotopic composition and O_2/Ar ratios within the CDISK4
575 dataset argue against this possibility. We therefore hypothesize that the anomalously low $^{17}\Delta$

values observed in the equatorial Pacific at low O_2 saturation may reflect previously unidentified analytical artifacts at low O_2/Ar ratios (Yeung et al., 2018).

4.1.3 Mass-dependent fractionation

The measured and modeled isotopic covariations are compared in Fig. 8D-F. In general, respiration and mixing create mass-dependent trends on the cross plots that depart from Rayleigh fractionation trends and express limited curvature. The data and isopycnal model are qualitatively consistent, but there are notable quantitative discrepancies we will describe below.

For the $^{17}\Delta$ vs. $\delta^{18}O$ plot (Fig. 8D), observed excesses in $^{17}\Delta$ values can be explained by primary productivity elevating $^{17}\Delta$ values by tens of ppm in the mixed layer and by a larger amount in the seasonal thermocline (Nicholson et al., 2014). The prescribed mass-dependent slope relating the $^{17}O/^{16}O$ and $^{18}O/^{16}O$ fractionations due to respiration (i.e., $\theta_{17/18,resp} = 0.520$) can explain the observed isotopic trend as $\delta^{18}O$ values increase. By contrast, for the Δ_{36} vs. $\delta^{18}O$ plot (Fig. 8E), the trend in the data is steeper than that predicted by the model, implicating the influence of diapycnal mixing or an underestimate of $\theta_{36/34,resp}$: the slope defined by the data resembles that of the 1% – 100% two-endmember mixing curve. Similarly, the trend in $^{17}\Delta$ and Δ_{36} values at high Δ_{36} values (Fig. 8F) requires a either diapycnal mixing or a larger $\theta_{36/34,resp}$ value to explain. These observations imply that the mass-dependent respiration slope relating $^{18}O^{18}O/^{16}O^{16}O$ and $^{16}O^{18}O/^{16}O^{16}O$ fractionation in the ocean may be larger than the slope prescribed in the model (i.e., $\theta_{36/34,resp} > 2.048$)—at least at greater depths in the aphotic zone.

First-principles calculations on active-site analogues of the cyctochrome *c* oxidase enzyme suggest that the intrinsic $\theta_{36/34,resp}$ value for respiration could be as high as ~2.1 (Ash et

al., 2020); the corresponding Rayleigh fractionation trajectory is shown in Fig. 8C ("Rayleigh II"). A larger $\theta_{36/34,resp}$ value could characterize marine systems, which have different oxygen consumption mechanisms from freshwater systems (from which the empirical estimate of $\theta_{36/34,resp}$ = 2.048 is derived). Note that the model used in this study included only a simple representation of respiratory oxygen consumption that did not partition contributions from individual mechanisms such as alternative (e.g., cyanide-resistant) oxidases or the Mehler reaction.

4.2 Implications for the superoxide pathway for O_2 consumption

Sutherland et al., (2020a) recently suggested that dissolved superoxide (O_2^-) cycling could be an important and previously overlooked component of the oceanic oxygen budget. Here, we evaluate its potential influences the isotopic budget of O_2 in the Pacific ocean.

The marine source of superoxide is represented generically by reaction 11:

$$O_2 + e^- \rightleftharpoons O_2^- \quad (11)$$

This reaction represents the net contributions from photorespiration, the Mehler reaction and/or abiotic photochemical reactions in the photic zone (Sutherland et al., 2020a). The backwards reaction constitutes the electron-detachment loss pathway for superoxide. Superoxide destruction can also produce hydrogen peroxide, either alone or alongside an O_2 product, through the following reactions:

$$O_2^- + 2H^+ + e^- \rightarrow H_2O_2 \quad (12)$$

$$2O_2^- + 2H^+ \rightarrow H_2O_2 + O_2 \quad (13)$$

Hydrogen peroxide can further react with organic carbon (C_{org}) to yield dissolved inorganic carbon (DIC), water, and O_2:

$$2H_2O_2 + C_{org} \rightarrow CO_2 + 2H_2O \quad (14)$$

$$2H_2O_2 \rightarrow 2H_2O + O_2 \quad (15)$$

The reduction of superoxide to water and DIC is likely the most important superoxide sink affecting the isotopic composition of oxygen in the ocean because the other channels may not yield net consumption of O_2 or O=O bonds, resulting in negligible changes to the isotopic mass balance.

Here, we estimate the steady-state gross flux for superoxide decay in the open ocean near Hawai'i by using the pseudo-first-order decay equation:

$$\frac{d[O_2^-]}{dt} = k_{decay}[O_2^-] \quad (16)$$

where k_{decay} is the pseudo first-order decay rate coefficient, which was experimentally determined to be $0.0106^{+0.012}_{-0.006}$ s^{-1} [1σ; (Sutherland et al., 2020a)]. Superoxide concentrations in the surface ocean (10m) near Hawai'i are ~10 pM, among the lowest of those reported in the literature (Roe et al., 2016; Sutherland et al., 2020a). Assuming that superoxide production and decay rates are equal at steady state, we calculate that $3.4^{+3.9}_{-1.6}$ μmol O_2/kg seawater/yr must be consumed to maintain these concentrations of superoxide. Superoxide concentrations measured at depth are larger (e.g., ~60pM at 100 m), implying proportionately larger gross O_2 consumption rates in the aphotic zone. These implied O_2 consumption fluxes are equal to or larger than the respiration rates at similar depths in the oligotrophic ocean (e.g., 3 μmol O_2/kg seawater/yr reported here for σ_θ = 25.8 – 26.2).

639 However, not all superoxide cycling will lead to net O_2 destruction, as several pathways
640 (i.e., reactions 13 and 15) yield a return flux of O_2 and may not involve O=O bond scission. We
641 will therefore estimate the lower limit of irreversible O_2 consumption through the superoxide
642 pathway by examining the stoichiometries of reactions 12 – 15. If all superoxide cycles through
643 these reactions, one-quarter of its oxygen atoms are irreversibly consumed at a minimum, via
644 reactions 13 and 14: just one of the two superoxide molecules forms H_2O_2 in reaction 13 (the
645 other reverts to neutral O_2) and just one of the two H_2O_2 molecules makes H_2O in reaction 15
646 (the other reverts to neutral O_2). All other pathways lead to more net superoxide removal. The
647 minimum net O_2 removal rate via the superoxide pathway in the surface ocean near Hawai'i is
648 therefore $\frac{1}{4}(3.4^{+3.9}_{-1.6}) = 0.9^{+1.0}_{-0.5}$ μmol O_2/kg seawater/yr, about one-third the implied respiration
649 rate on the σ_θ = 25.8 – 26.2 isopycnal surface (3 μmol O_2/kg seawater/yr). In the aphotic zone,
650 the minimum would be sixfold larger, i.e., $5.1^{+5.8}_{-2.7}$ μmol O_2/kg seawater/yr, which is difficult to
651 reconcile with the low apparent respiration rates for the deep Pacific. These results suggest that
652 superoxide destruction via electron detachment (the reverse of eq. 11) is the most important
653 mechanism of superoxide removal in the oligotrophic Pacific. In regions characterized by higher
654 respiration rates such as the equatorial Pacific, however, superoxide destruction via reactions 12
655 – 15 could constitute an important component of the O_2 budget.

656 In principle, the stable isotopologues of dissolved O_2 should record fractionation due to
657 superoxide consumption. While the fractionation factors for superoxide formation have not yet
658 been measured, theoretical calculations suggest that the equilibrium isotopic fractionation
659 between O_2 and superoxide is characterized by $^{18}\alpha$ = 0.970, $\theta_{17/18}$ = 0.527, and $\theta_{36/34}$ = 2.027 at
660 10°C (Ash et al., 2020), while a kinetically controlled outer-sphere electron-transfer mechanism
661 would have $^{18}\alpha$ = 0.920, $\theta_{17/18}$ = 0.523, and $\theta_{36/34}$ = 2.060 at 10°C (Yeung & Hayles, 2021).

These fractionation factors suggest that O_2 consumption via the superoxide pathway would tend to increase $\delta^{18}O$ and $^{17}\Delta$ values in the O_2 pool relative to the isopycnal model results; the latter kinetic mechanism in particular has a mass dependence that yields a steeper Rayleigh-like trajectory for $^{17}\Delta$ values (Rayleigh II shown in Fig. 8B).

However, higher $\delta^{18}O$ and $^{17}\Delta$ values for a given O_2 saturation, manifest as more strongly upward-sloping trends, would exacerbate disagreements between the measurements and model of the northeast Pacific (Fig. 7). This tendency disfavors the possibility of a significant missing superoxide O_2 consumption pathway in the model: either the superoxide pathway of net O_2 consumption is negligible, or the measured O_2 respiration fractionation factors already include the superoxide degradation pathway implicitly. Therefore, the isotopic data in the aphotic oligotrophic Pacific are best explained if most superoxides react to reform O_2 without rupturing the O=O bond.

5. Conclusions

Our measurements and modeling of dissolved O_2 in the northeast oligotrophic Pacific suggests that $\delta^{18}O$, $^{17}\Delta$, and Δ_{36} values of dissolved O_2 trace oxygen cycling and transport in the subsurface ocean. The results broadly corroborate previous estimates of respiration rates in the deep Pacific ocean and provide constraints on mechanisms of isotopic fractionation in the aphotic zone.

In particular, our results lend field-based support for the respiratory mass dependence of isotopic fractionation reported in a recent study (Ash et al., 2020), which are significantly different from those typically used for oxygen cycling in the ocean (Bender, 2000; Juranek &

Quay, 2013; Luz & Barkan, 2000). These new respiratory fractionation factors comprehensively explain the CDISK4 data from the northeast Pacific and provide a simple framework for explaining previously published data from the Pacific, including the enigmatic trends reported for the equatorial region. The new steeper "triple-oxygen" mass dependence for respiration (i.e., $\theta_{17/18,resp} \approx 0.520$), now supported by experiments, theory, and field observations, suggests that elevated $^{17}\Delta$ values in the ocean cannot be uniquely ascribed to primary production and mixing; respiratory oxygen consumption comprises an important component of the triple-oxygen isotope budget, and thus must be disentangled from the primary production signal as well as the variations caused by eddy-diffusive and advective transport. Nevertheless, the preservation of surface signals in deep-ocean O_2 may have implications for proxy reconstructions of marine productivity based on seafloor archives such as manganese nodules (Sharp et al., 2018; Sutherland, et al. 2020b).

Moreover, the isotopic results imply that net O_2 consumption through the superoxide pathway may be minor compared to conventional respiratory O_2 consumption in the oligotrophic north Pacific. Alternately, the effects of superoxide cycling are implicitly included in laboratory measurements of respiratory oxygen consumption. Nearly all isotopic data are well described by an independently determined set of isotopic fractionation factors for respiration; any missing O_2 consumption pathway, if present, is subtle. While the data cannot rule out irreversible O_2 consumption via the superoxide pathway in the equatorial Pacific, the isotopic systematics for respiration and mixing described herein can explain the majority of the existing data from the subsurface equatorial Pacific without needing to employ a new O_2 consumption pathway.

In contrast to those for $\delta^{18}O$ and $^{17}\Delta$ values, the aphotic-zone trends in Δ_{36} values appear to be largely determined by the O_2 removal mechanism (i.e., respiration) and much less so by

707 presumed transport and mixing patterns in the deep ocean. This unique behavior of Δ_{36} values, in
708 addition to its sensitivity to the presence of photosynthetic O_2, might be useful for partitioning
709 the importance of competing O_2 cycling mechanisms within the deep ocean.

710

711 **Acknowledgements**

712 We thank D. P. Nicholson for sharing his triple-oxygen data compilation. This research
713 was supported by National Science Foundation grants OCE-1436590, 1533501, and 1559004.

714

715 **Code and data availability**

716 The MATLAB code for the two-gyre model can be found on GitHub
717 (https://github.com/liptds). The isotopic data can be found in the Biological and Chemical
718 Oceanography Data Management Office (BCO-DMO) database at https://www.bco-
719 dmo.org/dataset/753594/.

720

721

722

References:

Angert, A., Rachmilevitch, S., Barkan, E., & Luz, B. (2003). Effects of photorespiration, the cytochrome pathway, and the alternative pathway on the triple isotopic composition of atmospheric O2. *Global Biogeochemical Cycles*, *17*(1). https://doi.org/10.1029/2002GB001933

Arístegui, J., Agustí, S., & Duarte, C. M. (2003). Respiration in the dark ocean. *Geophysical Research Letters*, *30*(2). https://doi.org/10.1029/2002GL016227

Ash, J. L., Hu, H., & Yeung, L. Y. (2020). What Fractionates Oxygen Isotopes during Respiration? Insights from Multiple Isotopologue Measurements and Theory. *ACS Earth and Space Chemistry*, *4*(1), 50–66. https://doi.org/10.1021/acsearthspacechem.9b00230

Bauer, E., & Siedler, G. (1988). The relative contributions of advection and isopycnal and diapycnal mixing below the subtropical salinity maximum. *Deep Sea Research Part A. Oceanographic Research Papers*, *35*(5), 811–837.

Bender, M. L. (1990a). The δ18O of dissolved O2 in seawater: A unique tracer of circulation and respiration in the deep sea. *Journal of Geophysical Research: Oceans*, *95*(C12), 22243–22252. https://doi.org/10.1029/JC095iC12p22243

Bender, M. L. (1990b). The δ18O of dissolved O2 in seawater: A unique tracer of circulation and respiration in the deep sea. *Journal of Geophysical Research: Oceans*, *95*(C12), 22243–22252. https://doi.org/10.1029/JC095iC12p22243

Bender, M. L. (2000). Tracer from the Sky. *Science*, *288*(5473), 1977–1978. https://doi.org/10.1126/science.288.5473.1977

Benson, B. B., & Krause, D. (1984). The concentration and isotopic fractionation of oxygen dissolved in freshwater and seawater in equilibrium with the atmosphere1. *Limnology and Oceanography*, *29*(3), 620–632. https://doi.org/10.4319/lo.1984.29.3.0620

746 Cole, S. T., Wortham, C., Kunze, E., & Owens, W. B. (2015). Eddy stirring and horizontal diffusivity
747 from Argo float observations: Geographic and depth variability. *Geophysical Research Letters*,
748 *42*(10), 3989–3997. https://doi.org/10.1002/2015GL063827
749 Craig, H. (1969). Abyssal carbon and radiocarbon in the Pacific. *Journal of Geophysical Research (1896-*
750 *1977)*, *74*(23), 5491–5506. https://doi.org/10.1029/JC074i023p05491
751 Eiler, J. M. (2007). "Clumped-isotope" geochemistry—The study of naturally-occurring, multiply-
752 substituted isotopologues. *Earth and Planetary Science Letters*, *262*(3), 309–327.
753 https://doi.org/10.1016/j.epsl.2007.08.020
754 Feely, R. A., Sabine, C. L., Lee, K., Berelson, W., Kleypas, J., Fabry, V. J., & Millero, F. J. (2004).
755 Impact of Anthropogenic CO2 on the CaCO3 System in the Oceans. *Science*, *305*(5682), 362–
756 366. https://doi.org/10.1126/science.1097329
757 Feely, R. A., Sabine, C. L., Schlitzer, R., Bullister, J. L., Mecking, S., & Greeley, D. (2004). Oxygen
758 Utilization and Organic Carbon Remineralization in the Upper Water Column of the Pacific
759 Ocean. *Journal of Oceanography*, *60*(1), 45–52.
760 https://doi.org/10.1023/B:JOCE.0000038317.01279.aa
761 Glover, D. M., Jenkins, W. J., & Doney, S. C. (2011). Modeling Methods for Marine Science.
762 https://doi.org/10.1017/CBO9780511975721
763 Guy, R. D., Fogel, M. L., & Berry, J. A. (1993). Photosynthetic Fractionation of the Stable Isotopes of
764 Oxygen and Carbon. *Plant Physiology*, *101*(1), 37–47. https://doi.org/10.1104/pp.101.1.37
765 Haine, T. W. N., & Hall, T. M. (2002). A Generalized Transport Theory: Water-Mass Composition and
766 Age. *Journal of Physical Oceanography*, *32*(6), 1932–1946. https://doi.org/10.1175/1520-
767 0485(2002)032<1932:AGTTWM>2.0.CO;2
768 Haskell, W. Z., Prokopenko, M. G., Hammond, D. E., Stanley, R. H. R., & Sandwith, Z. O. (2017).
769 Annual cyclicity in export efficiency in the inner Southern California Bight: ANNUAL
770 CYCLICITY IN EXPORT EFFICIENCY. *Global Biogeochemical Cycles*.
771 https://doi.org/10.1002/2016GB005561

772 Helman, Y., Barkan, E., Eisenstadt, D., Luz, B., & Kaplan, A. (2005). Fractionation of the Three Stable
773 Oxygen Isotopes by Oxygen-Producing and Oxygen-Consuming Reactions in Photosynthetic
774 Organisms. *Plant Physiology*, *138*(4), 2292–2298. https://doi.org/10.1104/pp.105.063768
775 Hendricks, M. B., Bender, M. L., Barnett, B. A., Strutton, P., & Chavez, F. P. (2005). Triple oxygen
776 isotope composition of dissolved O2 in the equatorial Pacific: A tracer of mixing, production, and
777 respiration. *Journal of Geophysical Research: Oceans*, *110*(C12).
778 https://doi.org/10.1029/2004JC002735
779 Ito, T., Follows, M. J., & Boyle, E. A. (2004). Is AOU a good measure of respiration in the oceans?
780 *Geophysical Research Letters*, *31*(17). https://doi.org/10.1029/2004GL020900
781 Juranek, L. W., & Quay, P. D. (2010). Basin-wide photosynthetic production rates in the subtropical and
782 tropical Pacific Ocean determined from dissolved oxygen isotope ratio measurements. *Global*
783 *Biogeochemical Cycles*, *24*(2). https://doi.org/10.1029/2009GB003492
784 Juranek, L. W., & Quay, P. D. (2013). Using Triple Isotopes of Dissolved Oxygen to Evaluate Global
785 Marine Productivity. *Annual Review of Marine Science*, *5*(1), 503–524.
786 https://doi.org/10.1146/annurev-marine-121211-172430
787 Juranek, L. W., Quay, P. D., Feely, R. A., Lockwood, D., Karl, D. M., & Church, M. J. (2012). Biological
788 production in the NE Pacific and its influence on air-sea CO2 flux: Evidence from dissolved
789 oxygen isotopes and O2/Ar. *Journal of Geophysical Research: Oceans*, *117*(C5).
790 https://doi.org/10.1029/2011JC007450
791 Karl, D. M., & Knauer, G. A. (1984). Vertical distribution, transport, and exchange of carbon in the
792 northeast Pacific Ocean: evidence for multiple zones of biological activity. *Deep Sea Research*
793 *Part A. Oceanographic Research Papers*, *31*(3), 221–243. https://doi.org/10.1016/0198-
794 0149(84)90103-1
795 Knox, M., Quay, P. D., & Wilbur, D. (1992). Kinetic isotopic fractionation during air-water gas transfer
796 of O2, N2, CH4, and H2. *Journal of Geophysical Research: Oceans*, *97*(C12), 20335–20343.
797 https://doi.org/10.1029/92JC00949

798 Koeve, W., Wagner, H., Kähler, P., & Oschlies, A. (2015). ^{14}C-age tracers in global ocean circulation
799 models. *Geoscientific Model Development*, *8*(7), 2079–2094. https://doi.org/10.5194/gmd-8-
800 2079-2015
801 Levine, N. M., Bender, M. L., & Doney, S. C. (2009). The δ18O of dissolved O2 as a tracer of mixing
802 and respiration in the mesopelagic ocean. *Global Biogeochemical Cycles*, *23*(1).
803 https://doi.org/10.1029/2007GB003162
804 Li, B., Yeung, L. Y., Hu, H., & Ash, J. L. (2019). Kinetic and equilibrium fractionation of O2
805 isotopologues during air-water gas transfer and implications for tracing oxygen cycling in the
806 ocean. *Marine Chemistry*. https://doi.org/10.1016/j.marchem.2019.02.006
807 Luz, B., & Barkan, E. (2000a). Assessment of Oceanic Productivity with the Triple-Isotope Composition
808 of Dissolved Oxygen. *Science*, *288*(5473), 2028–2031.
809 https://doi.org/10.1126/science.288.5473.2028
810 Luz, B., & Barkan, E. (2000b). Assessment of Oceanic Productivity with the Triple-Isotope Composition
811 of Dissolved Oxygen. *Science*, *288*(5473), 2028–2031.
812 https://doi.org/10.1126/science.288.5473.2028
813 Luz, B., & Barkan, E. (2005). The isotopic ratios 17O/16O and 18O/16O in molecular oxygen and their
814 significance in biogeochemistry. *Geochimica et Cosmochimica Acta*, *69*(5), 1099–1110.
815 https://doi.org/10.1016/j.gca.2004.09.001
816 Luz, B., & Barkan, E. (2009). Net and gross oxygen production from O2/Ar, 17O/16O and 18O/16O
817 ratios. *Aquatic Microbial Ecology*, *56*(2–3), 133–145. https://doi.org/10.3354/ame01296
818 Luz, B., & Barkan, E. (2011). Proper estimation of marine gross O2 production with 17O/16O and
819 18O/16O ratios of dissolved O2. *Geophysical Research Letters*, *38*(19).
820 https://doi.org/10.1029/2011GL049138
821 Matsumoto, K. (2007). Radiocarbon-based circulation age of the world oceans. *Journal of Geophysical*
822 *Research: Oceans*, *112*(C9). https://doi.org/10.1029/2007JC004095

Miller, M. F. (2002). Isotopic fractionation and the quantification of 17O anomalies in the oxygen three-isotope system: an appraisal and geochemical significance. *Geochimica et Cosmochimica Acta*, *66*(11), 1881–1889. https://doi.org/10.1016/S0016-7037(02)00832-3

Nicholson, D., Stanley, R. H. R., & Doney, S. C. (2014). The triple oxygen isotope tracer of primary productivity in a dynamic ocean model: Triple oxygen isotopes in a global model. *Global Biogeochemical Cycles*, *28*(5), 538–552. https://doi.org/10.1002/2013GB004704

Pack, A., Tanaka, R., Hering, M., Sengupta, S., Peters, S., & Nakamura, E. (2016). The oxygen isotope composition of San Carlos olivine on the VSMOW2-SLAP2 scale. *Rapid Communications in Mass Spectrometry*, *30*(13), 1495–1504. https://doi.org/10.1002/rcm.7582

Quay, P. D., Emerson, S., Wilbur, D. O., Stump, C., & Knox, M. (1993). The δ18O of dissolved O2 in the surface waters of the subarctic Pacific: A tracer of biological productivity. *Journal of Geophysical Research: Oceans*, *98*(C5), 8447–8458. https://doi.org/10.1029/92JC03017

Reuer, M. K., Barnett, B. A., Bender, M. L., Falkowski, P. G., & Hendricks, M. B. (2007). New estimates of Southern Ocean biological production rates from O2/Ar ratios and the triple isotope composition of O2. *Deep Sea Research Part I: Oceanographic Research Papers*, *54*(6), 951–974. https://doi.org/10.1016/j.dsr.2007.02.007

Roe, K. L., Schneider, R. J., Hansel, C. M., & Voelker, B. M. (2016). Measurement of dark, particle-generated superoxide and hydrogen peroxide production and decay in the subtropical and temperate North Pacific Ocean. *Deep Sea Research Part I: Oceanographic Research Papers*, *107*, 59–69. https://doi.org/10.1016/j.dsr.2015.10.012

Sharp, Z. D., Wostbrock, J. A. G., & Pack., A. (2018). Mass-dependent triple oxygen isotope variations in terrestrial materials. *Geochemical Perspectives Letters*, *7*, 27-31. https://doi.org/10.7185/geochemlet.1815

Sonnerup, R. E. (2001). On the relations among CFC derived water mass ages. *Geophysical Research Letters*, *28*(9), 1739–1742. https://doi.org/10.1029/2000GL012569

Stolper, D. A., Fischer, W. W., & Bender, M. L. (2018). Effects of temperature and carbon source on the isotopic fractionations associated with O2 respiration for 17O/16O and 18O/16O ratios in E. coli. *Geochimica et Cosmochimica Acta*, *240*, 152–172. https://doi.org/10.1016/j.gca.2018.07.039

Sutherland, K. M., Wankel, S. D., & Hansel, C. M. (2020a). Dark biological superoxide production as a significant flux and sink of marine dissolved oxygen. *Proceedings of the National Academy of Sciences*, *117*(7), 3433–3439. https://doi.org/10.1073/pnas.1912313117

Sutherland, K. M., Wostbrock, J. A. G., Hansel, C. M., Sharp, Z. D., Hein, J. R., & Wankel, S. D (2020b). Ferromanganese crusts as recorders of marine dissolved oxyen. *Earth and Planetary Science Letters*, 533, 116057. https://doi.org/10.1016/j.epsl.2019.116057

Takahashi, T., Broecker, W. S., & Langer, S. (1985). Redfield ratio based on chemical data from isopycnal surfaces. *Journal of Geophysical Research: Oceans*, *90*(C4), 6907–6924. https://doi.org/10.1029/JC090iC04p06907

Wostbrock, J. A. G., Cano, E. J., & Sharp, Z. D. (2020a). An internally consistent triple oxygen isotope calibration of standards for silicates, carbonates and air relative to VSMOW2 and SLAP2. *Chemical Geology*, *533*, 119432. https://doi.org/10.1016/j.chemgeo.2019.119432

Yeung, L. Y., & Hayles, J. A. (2021). Climbing to the Top of Mount Fuji: Uniting Theory and Observations of Oxygen Triple Isotope Systematics. *Reviews in Mineralogy and Geochemistry*, *86*(1), 97–135. https://doi.org/10.2138/rmg.2021.86.03

Yeung, L. Y., Young, E. D., & Schauble, E. A. (2012). Measurements of 18O18O and 17O18O in the atmosphere and the role of isotope-exchange reactions. *Journal of Geophysical Research: Atmospheres*, *117*(D18). https://doi.org/10.1029/2012JD017992

Yeung, L. Y., Ash, J. L., & Young, E. D. (2015). Biological signatures in clumped isotopes of O2. *Science*, *348*(6233), 431–434. https://doi.org/10.1126/science.aaa6284

Yeung, L. Y., Murray, L. T., Ash, J. L., Young, E. D., Boering, K. A., Atlas, E. L., et al. (2016). Isotopic ordering in atmospheric O2 as a tracer of ozone photochemistry and the tropical atmosphere.

873 *Journal of Geophysical Research: Atmospheres, 121*(20), 12,541-12,559.
874 https://doi.org/10.1002/2016JD025455
875 Yeung, L. Y., Hayles, J. A., Hu, H., Ash, J. L., & Sun, T. (2018). Scale distortion from pressure baselines
876 as a source of inaccuracy in triple-isotope measurements. *Rapid Communications in Mass*
877 *Spectrometry*, *32*(20), 1811–1821. https://doi.org/10.1002/rcm.8247
878 Zweng, M.M, J.R. Reagan, J.I. Antonov, R.A. Locarnini, A.V. Mishonov, T.P. Boyer, H.E.
879 Garcia, O.K. Baranova, D.R. Johnson, D.Seidov, M.M. Biddle, 2013. *World Ocean Atlas*
880 *2013, Volume 2: Salinity.* S. Levitus, Ed., A. Mishonov Technical Ed.; NOAA Atlas
881 NESDIS 74, 39 pp.

882
883
884
885
886
887
888

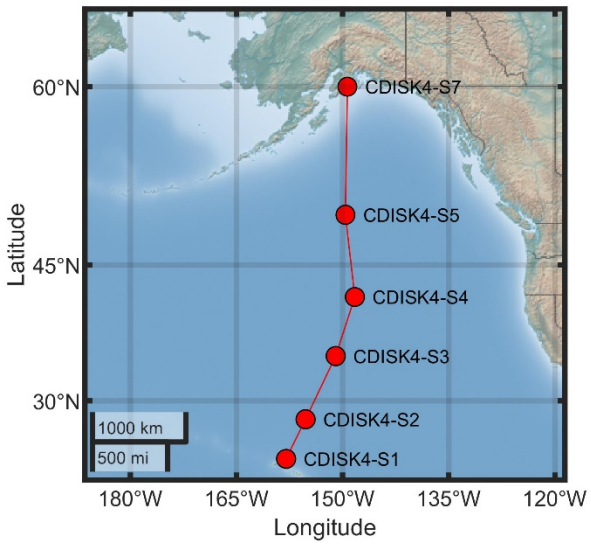

Fig. 1. Map of CDISK4 Stations where depth profiles were obtained. CDISK4-S1 is the same location as the Hawai'i Ocean Time Series site.

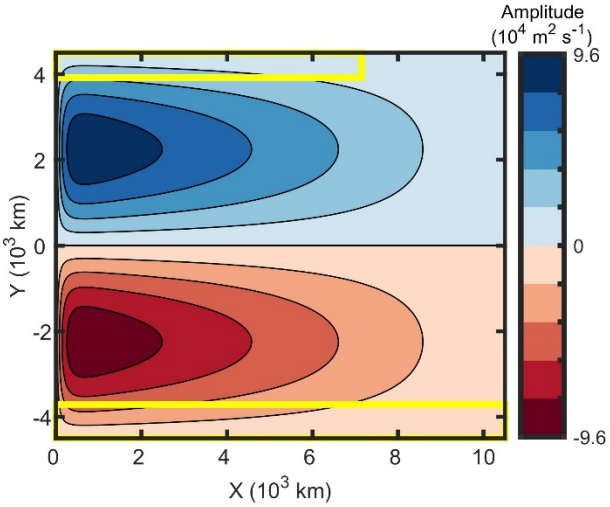

Fig. 2. Contour plot of the stream functions in the northern and southern gyres. In the northern gyre, the flow is clockwise, while in the southern gyre, the flow is counter-clockwise. The yellow boxes show the exposure surfaces where the isopycnal layer is ventilated at the northern and southern boundaries.

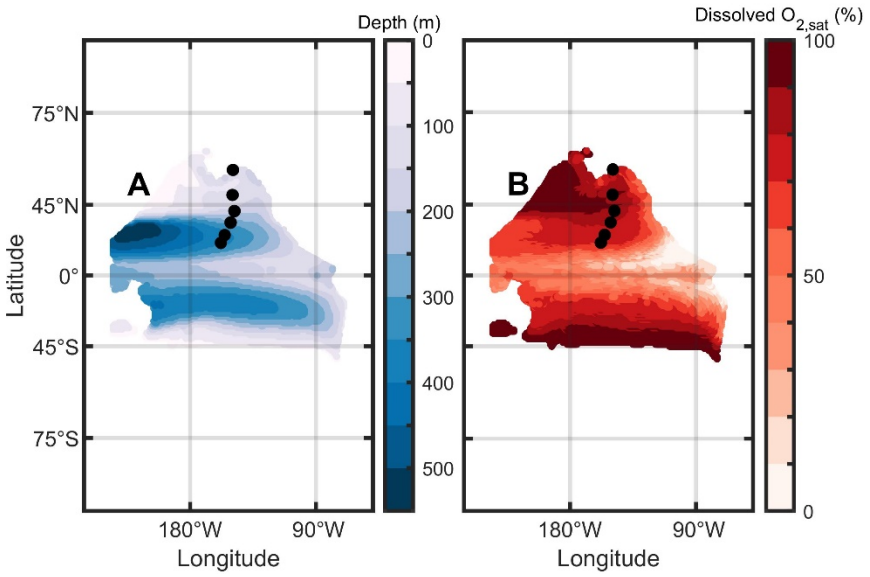

Fig. 3. Depth (left) and O_2 saturation (right) contour plots for the σ_θ = 25.8 - 26.2 layer derived from WOA 2013 data, shown with sampling locations overlain.

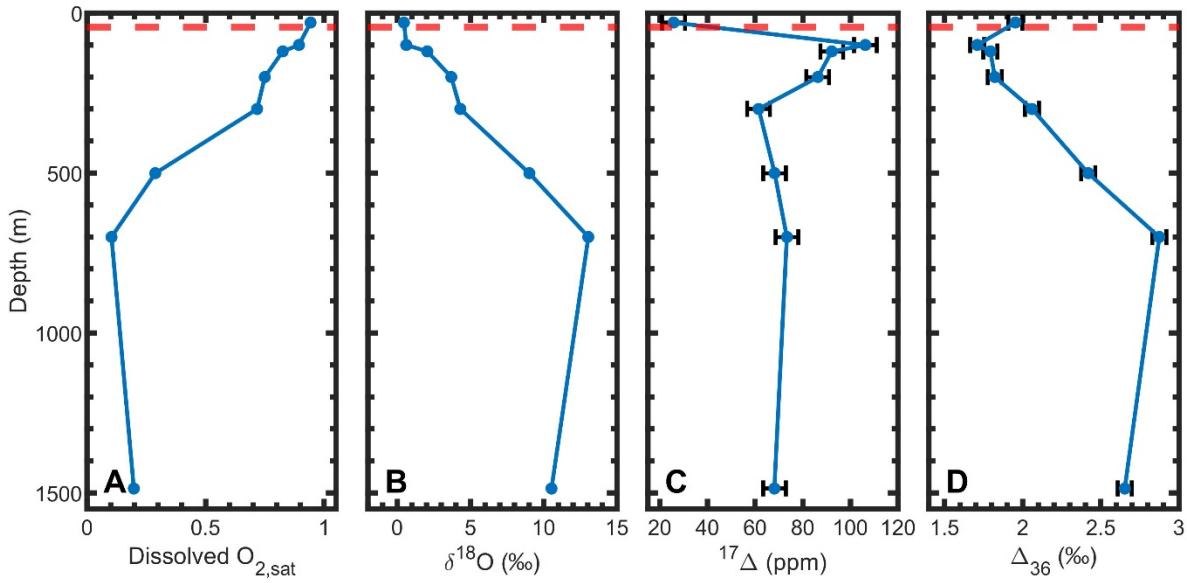

Fig. 4. Measured O_2 saturation and isotopologue composition vs depth at CDISK4-S1. The red horizontal line represents the mixed-layer depth. The data shown are (A) dissolved O_2 saturation, (B) $\delta^{18}O$, (C) $^{17}\Delta$, and (D) Δ_{36} vs. depth.

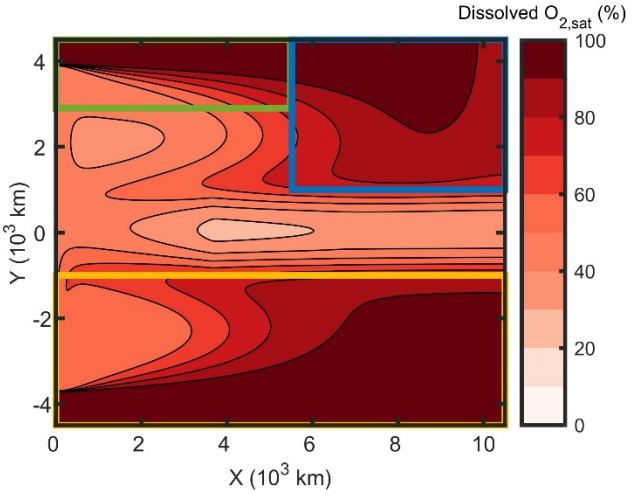

Fig. 5. Modeled dissolved O_2 saturation for the isopycnal layer with potential density σ_θ = 25.8 - 26.2. Three specific advection-diffusion regions are highlighted: the South Pacific gyre (yellow box), a portion of the Northeast Pacific (green box) and a portion of the Northwest Pacific (blue box).

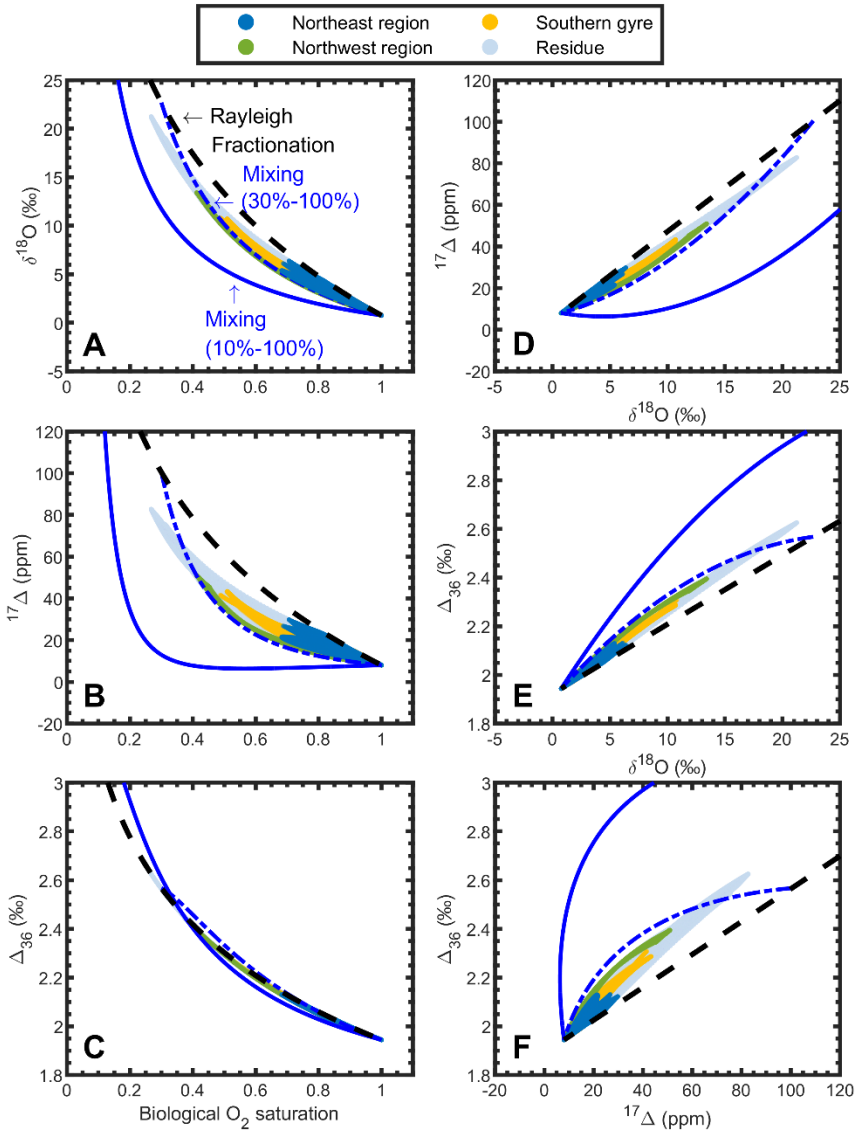

Fig. 6. Respiration-transport modeling results for the σ_θ = 25.8 - 26.2 isopycnal layer. The colors correspond to the boxed regions in Fig. 5. The black dashed line is the Rayleigh fractionation trend for closed-system respiration ($^{18}\alpha_{resp}$ = 0.982, $\theta_{17/18}$ = 0.520, $\theta_{36/18}$ = 2.048), starting from air-water saturation equilibrium. The blue solid and dot-dashed lines are a the two-end member mixing curves between air-water saturation equilibrium and a purely Rayleigh-fractionated low-O_2 endmember (10% or 30% O_2 saturation, respectively).

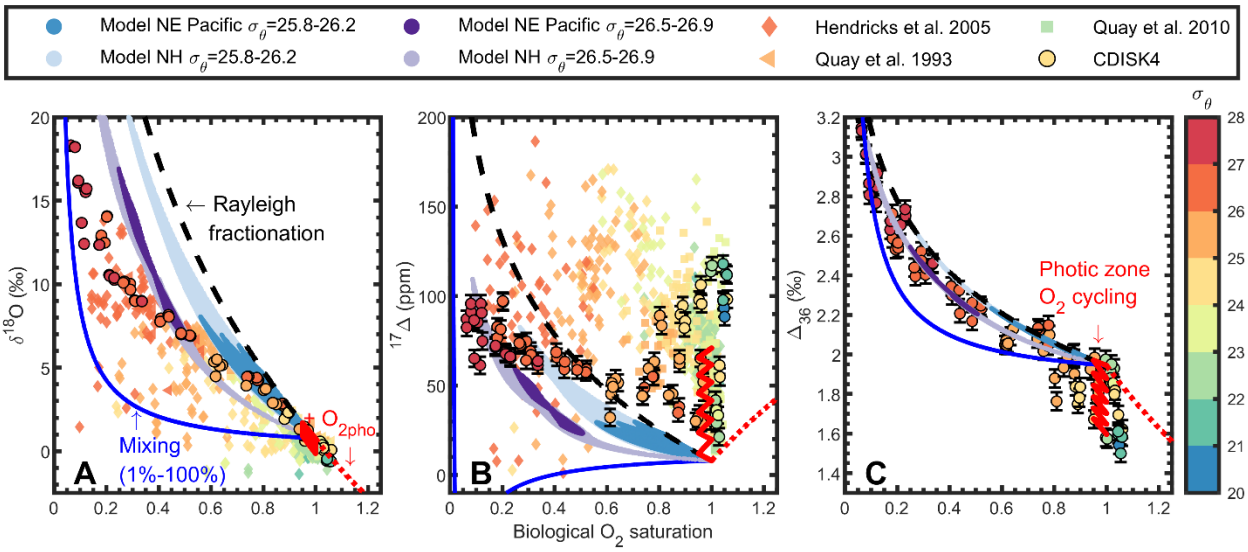

Fig. 7. Comparison of respiration-transport modeling results for the σ_θ = 25.8 - 26.2 and 26.5 - 26.9 isopycnal layers with the observations from CDISK4. Error bars correspond to the pooled standard deviation (±1σ). The pooled standard deviations for $\delta^{18}O$ values are smaller than the size of the data points. In the legend, *Model NE Pacific* corresponds to model results contained within the blue box in Fig. 5, whereas *Model NH* corresponds to results contained within the model northern hemisphere extratropics (i.e., Y > 1000km). The red "zig-zag" curve depicts a hypothetical trajectory associated with multiple cycles of mixed-layer O_2 production and consumption (labeled as *Photic zone O_2 cycling*).

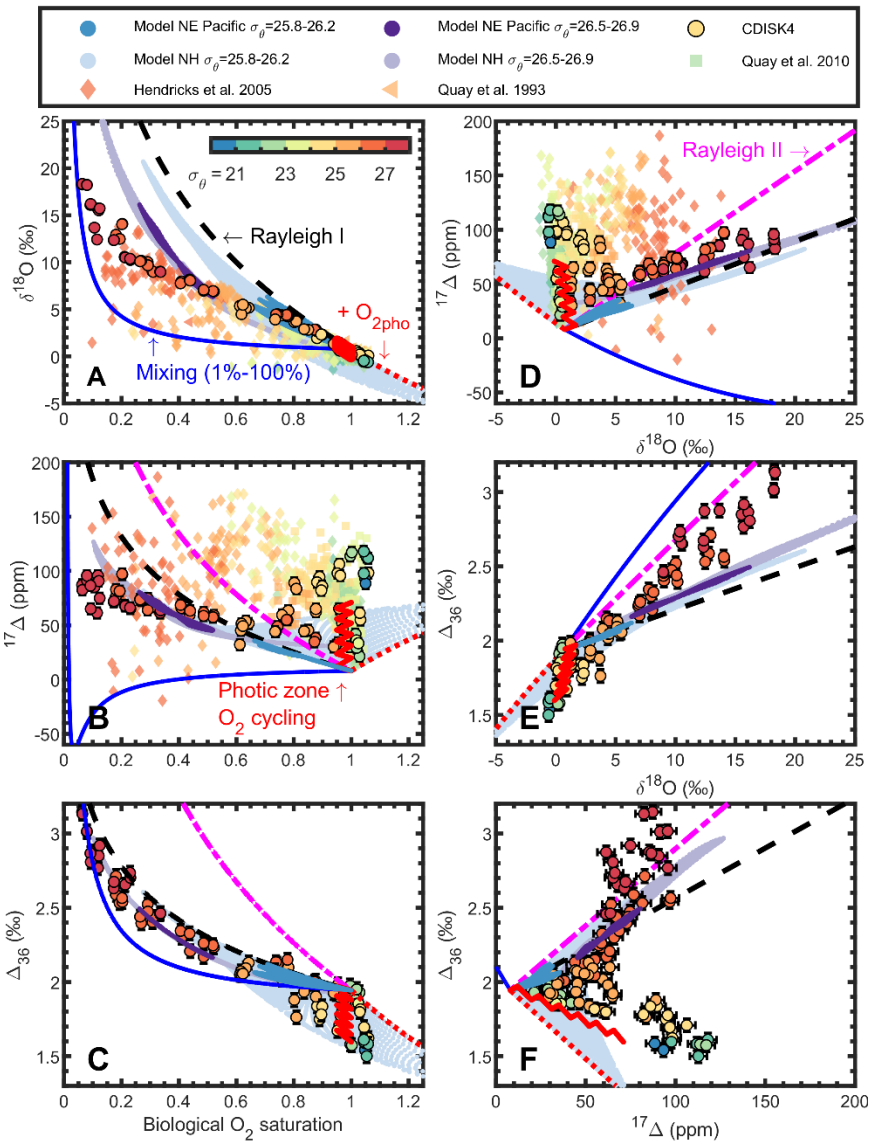

Fig. 8. Measurement-model comparison for the isopycnal model with photosynthetic O_2. For the σ_θ = 25.8 – 26.2 surface, the effects of photosynthesis shown are for the "explicit addition" method described in Section 2.3.4, to better capture the range in variability. For the σ_θ = 26.5 – 26.9 surface, the effects of photosynthesis shown are for the "implicit addition" method. "Implicit addition" results for the σ_θ = 25.8 – 26.2 surface are shown in Fig. S5. The colored curves are the same as in Fig. 7, with "Rayleigh I" corresponding to the pure Rayleigh fractionation trajectory for the fractionation factors used in the model ($^{18}\alpha_{resp}$ = 0.982, $\theta_{17/18,\,resp}$ = 0.520, and $\theta_{36/18,\,resp}$ = 2.048) and "Rayleigh II" corresponding to the sensitivity tests described in Section 4.1 and 4.2 (i.e., $\theta_{17/18,\,resp}$ = 0.523 and $\theta_{36/18,\,resp}$ = 2.1).

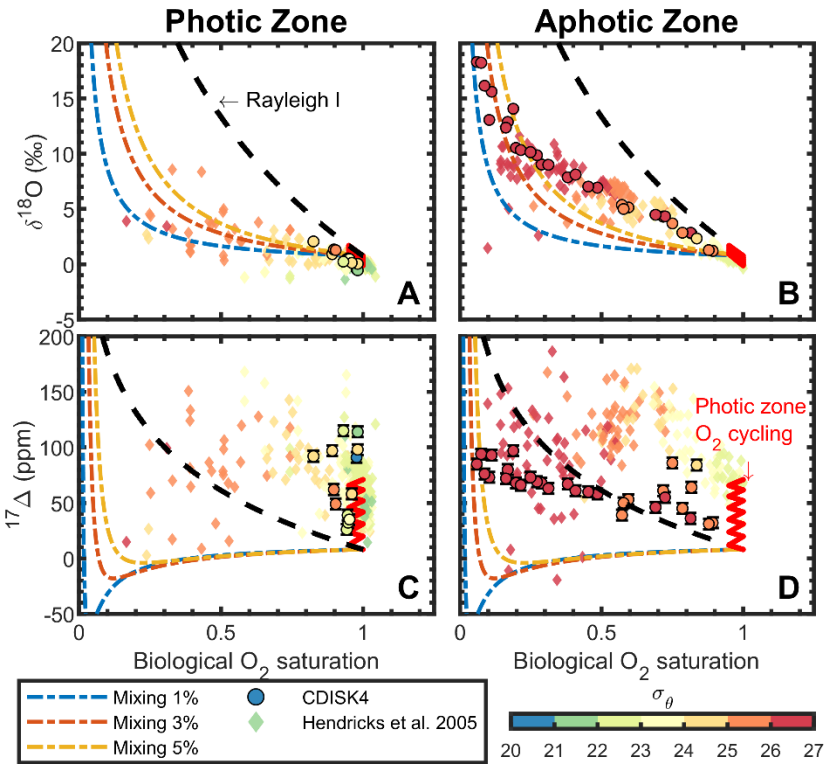

982

983 **Fig. 9.** O_2 isotopologue versus O_2 saturation for photic-zone and aphotic zone samples in the

984 CDISK4 data and those of Hendricks et al., (2005) compared to mixing and Rayleigh

985 fractionation scenarios.

986

Parameter	Respiration	Reference	Equilibrium	Reference
$^{18}\alpha$	0.982	(Bender, 1990)	1.00076	(Benson & Krause, 1984)
$\theta_{17/18}$	0.5200	(Ash et al., 2020)	0.5312	(Li et al., 2019)
$\theta_{36/18}$	2.048	(Ash et al., 2020)	1.9393	(Li et al., 2019)

987 Table 1. Respiration and equilibrium fractionation factors for O_2 isotopologues.

Parameters	Description	Value
A	Streamfunction amplitude	7.2×10^5 m^2/s
K	Isotropic diffusion coefficient	1200 m^2/s (5040, 3200, and 4000 m^2/s at western, central, and eastern equatorial boundary)
$\mathbf{J_{equator}}$	Mean O_2 respiration rate at equator	47 μmol/kg/yr
$\mathbf{J_{resp}}$	Mean O_2 respiration rate outside the equator	3.0 μmol/kg/yr

Table 2. Optimal parameter set determined from the region-specific grid search.